Human *CRB1*-Associated Retinal Degeneration: Comparison with the *rd8 Crb1*-Mutant Mouse Model

Tomas S. Aleman,[1] *Artur V. Cideciyan,*[1] *Geoffrey K. Aguirre,*[2] *Wei Chieh Huang,*[1] *Cristina L. Mullins,*[1] *Alejandro J. Roman,*[1] *Alexander Sumaroka,*[1] *Melani B. Olivares,*[1] *Frank F. Tsai,*[1] *Sharon B. Schwartz,*[1] *Luk H. Vandenberghe,*[3] *Maria P. Limberis,*[3] *Edwin M. Stone,*[4] *Peter Bell,*[3] *James M. Wilson,*[3] *and Samuel G. Jacobson*[1]

Purpose. To investigate the human disease due to *CRB1* mutations and compare results with the *Crb1*-mutant *rd8* mouse.

Methods. Twenty-two patients with *CRB1* mutations were studied. Function was assessed with perimetry and electroretinography (ERG) and retinal structure with optical coherence tomography (OCT). Cortical structure and function were quantified with magnetic resonance imaging (MRI). *Rd8* mice underwent ERG, OCT, and retinal histopathology.

Results. Visual acuities ranged from 20/25 to light perception. Rod ERGs were not detectable; small cone signals were recordable. By perimetry, small central visual islands were separated by midperipheral scotomas from far temporal peripheral islands. The central islands were cone mediated, whereas the peripheral islands retained some rod function. With OCT, there were small foveal islands of thinned outer nuclear layer (ONL) surrounded by thick delaminated retina with intraretinal hyperreflective lesions. MRI showed structurally normal optic nerves and only subtle changes to occipital lobe white and gray matter. Functional MRI indicated that whole-brain responses from patients were of reduced amplitude and spatial extent compared with those of normal controls. *Rd8* mice had essentially normal ERGs; OCT and histopathology showed patchy retinal disorganization with pseudorosettes more pronounced in ventral than in dorsal retina. Photoreceptor degeneration was associated with dysplastic regions.

Conclusions. *CRB1* mutations lead to early-onset severe loss of vision with thickened, disorganized, nonseeing retina. Impaired peripheral vision can persist in late disease stages. *Rd8* mice also have a disorganized retina, but there is sufficient photoreceptor integrity to produce largely normal retinal function. Differences between human and mouse diseases will complicate proof-of-concept studies intended to advance treatment initiatives. (*Invest Ophthalmol Vis Sci.* 2011;52:6898–6910) DOI: 10.1167/iovs.11-7701

From the [1]Scheie Eye Institute, Department of Ophthalmology, the [2]Department of Neurology, and the [3]Gene Therapy Program, Department of Pathology and Laboratory Medicine, University of Pennsylvania, Philadelphia, Pennsylvania; and the [4]Howard Hughes Medical Institute and Department of Ophthalmology, University of Iowa Carver College of Medicine, Iowa City, Iowa.

Supported by grants from Foundation Fighting Blindness, Macula Vision Research Foundation, Hope for Vision, The Chatlos Foundation, and The NU Fund for Retinal Research. AVC is an RPB Senior Scientific Investigator.

Submitted for publication April 6, 2011; revised July 2, 2011; accepted July 5, 2011.

Disclosure: **T.S. Aleman**, None; **A.V. Cideciyan**, None; **G.K. Aguirre**, None; **W.C. Huang**, None; **C.L. Mullins**, None; **A.J. Roman**, None; **A. Sumaroka**, None; **M.B. Olivares**, None; **F.F. Tsai**, None; **S.B. Schwartz**, None; **L.H. Vandenberghe**, None; **M.P. Limberis**, None; **E.M. Stone**, None; **P. Bell**, None; **J.M. Wilson**, None; **S.G. Jacobson**, None

Corresponding author: Samuel G. Jacobson, Scheie Eye Institute, University of Pennsylvania, 51 N. 39th Street, Philadelphia, PA 19104; jacobsos@mail.med.upenn.edu.

There has been longstanding scientific interest in Crumbs proteins, originating from discoveries in *Drosophila;* in mammals, there are several homologues of Crumbs (reviewed in Ref. 1). CRB1 is thought to be expressed in Müller glial (MG) cells and localizes at a subapical region near intercellular adherens junctions between photoreceptors and MG cells at the outer limiting membrane (OLM). Mutations in the *CRB1* gene cause an autosomal recessive early-onset retinal degeneration characterized by abnormal retinal organization and severe visual loss.[2–7] Results to date in patients with *CRB1*-associated retinal degenerations (*CRB1*-RD), taken together with findings in experimental animals, support the conjecture that *CRB1* mutations result in retinal maldevelopment and progressive degeneration.[5,8] There is also experimental evidence supporting a role for *CRB1* in the maintenance of photoreceptor integrity.[8,9]

Major progress was made recently when gene replacement therapy for another recessive early-onset retinal degeneration, the *RPE65* form of Leber congenital amaurosis (LCA), was shown to be safe and efficacious in early-phase clinical trials (reviewed in Ref. 10). One of the important challenges facing the field of retinal degenerations is how to expand the recent gene therapy success in *RPE65*-LCA to dozens of other molecular forms of retinitis pigmentosa (RP) and LCA with different pathophysiological mechanisms. It remains unclear whether *CRB1*-RD patients are candidates for such emerging therapies. In this work we used psychophysics, retinal imaging, and cortical imaging to increase understanding of the disease effects associated with *CRB1*-RD, with the ultimate goal of assessing the relevance of treatment strategies to this group of patients. In addition, we made a side-by-side comparison of the human retinopathy with that of the retinal disease in the *rd8* mouse, a naturally occurring *Crb1* mutant. The results of this comparison are a key issue for proof-of-concept studies.

Materials and Methods

Human Subjects

The study included 22 patients with *CRB1* mutations (Table 1). Institutional review board approval and informed consent were obtained before the study, and the procedures adhered to the tenets of the Declaration of Helsinki.

TABLE 1. Clinical and Molecular Characteristics of the *CRB1* Patients

Patient	Age at First Visit (y/Sex)	*CRB1* Mutation		Visual Acuity*	Refraction†	Fundus Features‡	Kinetic Visual Field Extent (V-4e)§	ERG Amplitude‖		Reference
		Allele 1	Allele 2					Rod b-Wave	Cone Flicker	
P1	0.6/F	p.Cys948Tyr	Deletion of *CRB1*	F&FL	+6.50	Granular	NP	ND	11	4, 5, 7
P2	4/M	p.Cys948Tyr	p.Ser1350 del1	20/100	+6.00	Granular	7	ND	ND	4, 5, 7, 45
P3	5/F	p.Glu204 del7	p.Cys480Arg	20/200	+6.50	Granular; white dots	NP	ND	10	7
P4	8/F	p.Cys948Tyr	p.Cys1218Phe	20/30	+5.50	Granular; PPRPE	30	ND	7	4, 5, 7, 45
P5¶	9/F	p.Arg764Cys	p.Val1336Ile	20/800	+3.50	Clumped and bone-spicule pigment; macular pigmentary changes#	12	ND	ND	4, 5, 7
P6	13/F	p.Cys948Tyr	p.Cys948Tyr	20/63	+4.75	Granular; PPRPE; macular pigmentary changes	7	ND	<1	
P7	13/M	p.Cys948Tyr	p.Gln335Pro	20/30	+5.25	Bone-spicule pigment; granular	87	ND	13	
P8¶	18/F	p.Arg764Cys	p.Val1336Ile	20/63	+1.25	Bone-spicule pigment; white dots	30	ND	1	4, 5, 7, 45
P9	20/M	p.Cys948Tyr	p.Cys948Tyr	20/80	+1.00	Clumped pigment#	3	ND	ND	
P10¶	22/M	p.Val578Glu	p.Val578Glu	20/400	+4.50	Clumped pigment; macular pigmentary changes; white dots	4	ND	7	7
P11	25/F	p.Cys948Tyr	p.Cys948Tyr	20/200	+8.75	Clumped pigment; macular pigmentary changes	8	ND	ND	7
P12	25/M	p.Pro748 del3	p.Pro748 del3	20/125	+2.00	Clumped pigment; white and yellow dots	8	ND	<1	4, 5, 7, 45
P13	26/M	p.Arg764Cys	p.Arg764Cys	20/40	+0.75	Bone-spicule pigment; white and yellow dots	35	ND	4	
P14	26/F	p.Ile852Thr	p.Leu1097Arg	LP	+9.25	Clumped pigment; macular pigmentary changes	ND	ND	ND	
P15¶	27/F	p.Gly477Arg	p.Arg764Cys	20/300	+3.50	Clumped and bone-spicule pigment; macular pigmentary changes; white and yellow dots	45	ND	5	
P16¶	27/M	p.Val578Glu	p.Val578Glu	20/1600**	+6.75	Clumped pigment; macular pigmentary changes; white dots	<1	ND	<1	7
P17	29/F	p.Cys85 ins2	p.Thr745Met	20/800	+5.25	Clumped pigment; macular pigmentary changes	20	ND	3	5, 7
P18	34/F	p.Cys383Tyr	p.Asn871 ins1	CF	+6.25	Clumped pigment; macular atrophy	2	ND	2	4, 5
P19	38/M	p.Cys948Tyr	p.Trp1370Cys	20/70	+1.00	Bone-spicule pigment; white dots	61	ND	8	
P20	44/M	p.Cys948Tyr	p.Cys587Tyr	HM	+7.00	Clumped pigment; macular pigmentary changes	ND	ND	ND	
P21¶	47/F	p.Gly477Arg	p.Arg764Cys	20/50	Pseudophakia	Granular; clumped pigment	37	NP	NP	
P22	48/M	p.Lys801X	p.Leu1074Ser	LP**	Pseudophakia	Bone-spicule pigment; macular atrophy#	ND	ND	ND	5, 7

PPRPE, preserved para-arteriole retinal pigment epithelium; ND, not detectable; NP, not performed; F&FL, fixes and follows light; CF, counts fingers; HM, hand motion; LP, light perception.

* Best corrected visual acuity (eye with better acuity).

† Spherical equivalent.

‡ All had vitreous cells, attenuated retinal vessels, and various degrees of waxy appearance of the optic nerve head.

§ Expressed as a percentage of normal mean of V-4e target; 2 SD below normal is 90%[13]; average both eyes; similar in the two eyes unless specified.

‖ Expressed as a percentage of normal mean amplitude (rod = 292 μV; cone flicker = 172 μV); 2 SD below normal is 67% for rod b-wave and 60% for cone flicker.[14]

¶ Indicates sibling pairs: P5 and P8, P10 and P16, P15 and P21.

Coats disease.

** Keratoconus.

Visual Function

Patients underwent a complete eye examination, electroretinography (ERG), and Goldmann kinetic visual field testing. Static computerized perimetry was performed with 1.7° diameter, 200-ms duration stimuli under dark-adapted (500- and 650-nm stimuli) and light-adapted (600 nm) conditions. A full-field test of 72 loci on a 12° grid and a horizontal profile across the fovea (extending 60° at 2° intervals) were used. Photoreceptor mediation was determined by the sensitivity difference between detection of the 500- and 650-nm stimuli.[11] Rod sensitivity loss (500 nm, dark-adapted) at each test locus was calculated by comparison with normal mean sensitivity at that location. Loci were considered to have no measurable rod sensitivity if loss was >30 dB.[12] Cone-mediated function from dark-adapted perimetry was compared with normal results measured during the cone plateau of dark adaptation. Techniques, methods of data analysis, and normal results for ERGs and perimetry have been published.[11,13,14]

Optical Coherence Tomography

Retinal cross sections were obtained with OCT. Most data collection used a spectral-domain (SD) OCT system (RTVue-100; Optovue Inc., Fremont, CA); a minority of patients were examined with earlier OCT instruments (OCT1 and OCT3; Carl Zeiss Meditec, Dublin, CA). Post-acquisition processing of OCT data was performed with custom programs (MatLab 6.5; MathWorks, Natick, MA). For topographic analysis, the precise location and orientation of each scan relative to retinal features (blood vessels, optic nerve head) were determined using video images of the fundus. Longitudinal reflectivity profiles (LRPs) were allotted to regularly spaced bins in a rectangular coordinate system centered at the fovea; the waveforms in each bin were aligned and averaged. For two-dimensional maps, 0.3×0.3-mm bins were used for sampling whereas 0.15-mm bins were used for analysis along the vertical meridian. Missing data were interpolated bilinearly; thickness values were mapped to a pseudocolor scale; and fundus landmarks were overlaid for reference. Our recording and analysis techniques have been published.[5,15–18] Cross-sectional images were also compared with en face infrared images to determine the relationship of intraretinal hyperreflective OCT lesions to pigmentary lesions on funduscopy. In a subset of patients, OCT 3D macular raster scans (Optovue) were reconstructed in an en face view to examine for pigmentary changes. Raster scans containing pigmentary changes were registered with 30-degree infrared reflectance images to determine the relation between the reflective properties and the location of the pigment.

Magnetic Resonance Imaging

A 3.0-Tesla MRI system (Trio; Siemens Healthcare, Washington, DC) and an eight-channel head coil were used for MRI acquisition. The intraorbital optic nerve diameter was assessed by direct measurement of the interpial diameter of the optic nerve on high-resolution (0.375 × 0.375 × 2.2 mm), T2-weighted anatomic images. Voxel-based morphometry[19] was performed on the log Jacobian measure obtained after diffeomorphic warping[20] of the T1-weighted, MPRAGE (1 mm isotropic) images of patients and a group of normal subjects to a representative brain image. The average deformation score was also obtained for normal subjects and patients from within a region of interest defined within occipital lobe white matter. Cortical gray matter thickness was assessed using FreeSurfer (http://surfer.nmr.mgh.harvard.edu/; Athinoula A. Martinos Center for Biomedical Imaging, Charlestown, MA) within a V1 region of interest defined by cortical surface topology.[21] Functional neural response to light stimulation was measured using BOLD echoplanar images (3 × 3 × 3-mm resolution over 30 slices at TR of 3 seconds) during two 7-minute scans. A white rectangular screen (subtending 27° × 18°) of uniform luminance and flickering at 5 Hz was presented for 30-second periods, alternated with 30-second periods of darkness. The maximum screen luminance was 3.75 log cd · m^{-2}; a 1-log unit neutral density filter was placed in the light pathway for controls for comfort. Stimulus-induced changes in the BOLD signal were modeled as a boxcar covariate, convolved with a population hemodynamic response function.[22] The percentage signal change associated with a level of visual stimulation (derived from the beta value-modeling BOLD signal change relative to the intercept term) was obtained for each voxel for each scan, and the average signal change across population calculated for each voxel in standard space. The absence of map-wise differences in hemispheric response allowed us to collapse the data from the two hemispheres to create a single pseudohemisphere. A region of interest was defined in standard space to include all posterior visual areas (both primary and association cortices), and the cortical volume that demonstrated a strong response to visual stimulation (>2% signal change) was identified.

Animals

Rd8 (*Crb1*^{rd8}) mice on a C57BL/6 background were obtained from The Jackson Laboratory (Bar Harbor, ME) and a colony of mice established. C57BL/6 wild-type (WT) mice served as controls. Animals were raised from birth in 12-hour-on/12-hour-off cyclic lighting (ambient illumination, <3 lux). Access to food and water was ad libitum. Procedures were conducted according to the ARVO Statement for the Use of Animals in Ophthalmic and Vision Research and with approval from the Institutional Animal Care and Use Committee of the University of Pennsylvania.

Electroretinography

Full-field ERGs were recorded as previously described.[23] The animals were anesthetized (ketamine HCl, 65 mg/kg and xylazine, 5 mg/kg) and the pupils dilated (tropicamide, 1%, and phenylephrine, 2.5%). ERG stimuli included increasing intensities of blue-light flashes (−4.2 to +0.1 log scot cd · s · m^{-2}, 0.3–0.5-log unit steps) in the dark-adapted state (>12 hours), white flashes of 0.4 log cd · s · m^{-2}, on a 25-cd · m^{-2} white background, and 15-Hz flicker of 0.4 log cd · s · m^{-2} on a 6 cd · m^{-2} background. Dark-adapted b-wave amplitudes were fit with a Naka-Rushton function[13,24] to obtain estimates of maximum amplitude (V_{max}) and semisaturation intensity (log K). Differences between WT (n = 37) and *rd8* (n = 26) mice were assessed for six ERG parameters in three age-matched groups, by means of *t*-tests corrected for multiple comparisons (α = 0.95). In a subset of the mice (n = 12 for *rd8; n* = 8 for WT), S- and M-opsin-mediated cone function was compared by using a pair of responses to ultraviolet (UV) and green stimuli presented in the light-adapted state (40 cd · m^{-2} white background), as previously described.[25,26] In short, green flashes were produced by an LED source (510-nm peak, 0.87-log cd · s · m^{-2}, 4-ms duration) and UV flashes were obtained from a filtered xenon source (360 nm peak). The intensity of the UV flash was chosen to produce responses matched in waveform to those elicited with the green flash in the WT mice. Both stimuli were presented in a ganzfeld lined with aluminum foil.[27]

Histology

The eyes were fixed immediately after enucleation in 2.5% glutaraldehyde and 2% paraformaldehyde in phosphate-buffered saline at room temperature for at least 24 hours, dehydrated with graded ethanol, and embedded in paraffin. Complete sectioning of whole eyes was performed through the vertical meridian from nasal to temporal. Sections (5-μm thickness) were collected at regular intervals from ~24 sites per eye, stained with hematoxylin and eosin, and photographed with an inverted microscope (Eclipse Ti-E; Nikon, Tokyo, Japan). Image-processing software (Photoshop 6.0; Adobe Systems, San Jose, CA) was used. Measurements of thickness of inner and outer segment layers (IS+OS) were made by outlining the OLM and RPE boundaries and measuring the distance between them at regular intervals over a 400-μm length. These measures were averaged to get the mean IS+OS thickness within the region imaged. Distances were quantified using linear distance–measuring software (Engauge digitizer, ver. 4.1; http://digitizer.sourceforge.net/ open source from Geeknet, Fairfax, VA) and a calibration target (Graticules, Ltd., Tonbridge, UK). Within a section, two adjacent regions were selected from the inferior (ventral) hemi-

sphere; in *rd8* eyes, one region was chosen to show dysplastic retina (at least two pseudorosettes per region), and the other showed no evident dysplasia.

Optical Coherence Tomography

Retinal cross-sections in WT and *rd8* mice were acquired with a 3.2 μm resolution SD-OCT system (Bioptigen, Inc., Durham, NC). Mice were anesthetized and the pupils dilated by the methods used for ERG (see above). Corneas were lubricated frequently during the imaging session (Systane Ultra ophthalmic lubricant; Alcon Ltd., Fort Worth, TX). Using the fast fundus mode (200 raster scans of 200 LRPs each), we first centered the location of the optic nerve head (ONH) within a 1.6 $\times$ 1.6-mm field of view by rotating the cassette that holds the animal. High-resolution (40 parallel raster scans of 1000 LRPs each repeated four times) scans were acquired along the horizontal (nasal–temporal) and vertical (dorsal–ventral) axes. The eyes were then repositioned for further scanning by placing the ONH near the top or bottom center of the view. High-resolution scans were repeated at these locations, for a total coverage of 3.2 mm. Each LRP had 1024 samples representing 1160 μm of retinal depth along the *z*-axis.

Postacquisition processing of OCT data was performed with commercial software (InVivoVue Clinic software; Bioptigen, Inc., and custom programs written in MATLAB 6.5; MathWorks, Natick, MA). Four repetitions of the high-resolution scans were averaged using the manufacturer's software. Vertical scans obtained superior and inferior to the center of the ONH were merged by custom programs. The LRPs of the merged OCT images were aligned by manually straightening the RPE reflection which was defined as the second hyperreflective band from the sclerad side.[28] Measurements of retinal thickness were performed between the vitreoretinal interface and the RPE peak.

Statistical Analysis

Human fMRI data comparisons were based on the one-tailed *t*-test. Mouse photoreceptor IS+OS thickness differences from histologic sections were evaluated with repeated-measures analyses of variance (ANOVA), including genotype (WT vs. *rd8*), age, and local retinal organization (dysplasia versus nondysplasia) as factors.

Results

The 22 patients (ages 7 months to 48 years at first visit) with *CRB1* mutations were from 19 unrelated families (Table 1). Most patients had been diagnosed as having LCA or early-onset retinal degeneration; patient (P)7, P13, P19, and P21 were diagnosed with RP. Hypermetropia was a common clinical finding (all 20 phakic patients). Coats disease was present in three patients (P5, P9, and P22), and there was keratoconus in two patients (P16 and P22). Fundus features included clumped and bone-spicule–like pigment, white and yellow lesions, and pigmentary changes in the macula (Table 1); PPRPE (preserved para-arteriole retinal pigment epithelium) was noted in two patients (P4 and P6).

Visual Function in *CRB1*-RD

CRB1-RD patients had visual acuities that ranged from 20/30 to LP; more than half of the patients in this cohort (13/21; 62%) had visual acuity of 20/100 or worse (Table 1). There was severe retina-wide dysfunction by ERG and perimetry. ERGs were detectable in 14 (67%) of 21 of the patients examined. There were no measurable rod b-waves but there were small cone-mediated signals (Table 1). Among the patients with measurable kinetic visual fields, a common pattern was a small, central island of vision separated from a peripheral temporal island by a complete annular midperipheral scotoma; some patients had only peripheral temporal islands as their remnant of vision.

Visual field abnormalities are illustrated in three representative patients (Fig. 1). P4 at age 14 showed a central island and a temporal peripheral island in response to the largest target (V-4e); perception of the small target (I-4e) was limited to the central few degrees. P8 at age 19 had a smaller central island, but there remained a large temporal island of function. P12 at age 28 had a very limited central island near fixation and a temporal field island (Fig. 1A). Rod and cone sensitivity losses across the visual field were mapped for these three patients (Fig. 1B). Consistent with the nondetectable rod ERGs in these and other *CRB1*-RD patients, the three patients lacked measurable rod function psychophysically across most of the visual field, except for small temporal peripheral islands in each case. Cone sensitivity loss maps show residual but impaired central and temporal peripheral cone islands. P12 has only a central island of cone function detectable. To define in more detail central rod- and cone-mediated function at relatively early disease stages, we measured dark-adapted sensitivity profiles with chromatic stimuli (500 and 650 nm) along the horizontal meridian (central 60°) in the same three patients (Fig. 1C) as well as in seven others (ages, 12–29 years). Even at the youngest ages examined with these stimuli (12 and 13 years), central visual function was abnormal. There was mainly cone-mediated detection of centrally presented stimuli; rod-mediated vision could be measured in loci around fixation in only three patients in the second decade of life and was reduced by at least ~2 log units. Normal cone sensitivity was measurable at the most central locations in a minority of patients; most patients had central islands of cone function, with sensitivity losses ranging from 0.5 to 2.5 log units.

Longitudinal data in P7 for an 11-year period (Fig. 2) provided a view of the progression of the disease to the stage with only central and peripheral islands. At age 13, kinetic visual fields with the V-4e target were relatively full in extent except for a scotoma in the inferior nasal field; the I-4e target was perceived only in the central field (Fig. 2A). From ages 15 to 24 years, there was progression of field loss from an incomplete absolute midperipheral scotoma (age 15) to a complete annular scotoma separating a central island from a temporal peripheral island (age 24). Maps of rod and cone sensitivity losses across the visual field (Fig. 2B) or as horizontal sensitivity profiles (Fig. 2C) also demonstrated progression. At age 13, there was a large midperipheral rod and cone scotoma that reached the nasal periphery and surrounded a small central island of reduced rod function but better cone function (Fig. 2B). By age 24, there was only a small island of abnormally reduced cone function with a retained temporal island of reduced (by at least 1.5 log unit) but detectable rod and cone function. Profiles of central visual function across the horizontal meridian (Fig. 2C) indicate that there was severely reduced but detectable extracentral rod function at age 13 (Fig. 2C, top); cone function had near normal sensitivity at fixation (Fig. 2C, bottom). Over the ensuing 11 years, rod function became undetectable and cone function progressively decreased in extent and sensitivity. P15 had longitudinal results spanning a 22-year interval (27–49 years). Perimetric results at age 27 were similar to those of P7 at age 15 but when seen again at age 49, the patient had only hand motions vision, and there was no detection of stimuli in kinetic or static perimetry.

Retinal and Visual Brain Structure in *CRB1*-RD

Maps of retinal thickness topography derived from OCT in patients with *CRB1*-RD illustrate the structural abnormalities in these patients (Fig. 3). The thickness map of the normal retina, from the retinal pigment epithelium (RPE) to the inner limiting membrane, shows some distinctive features (Fig. 3A, left): a central depression or foveal pit, a surrounding ring of in-

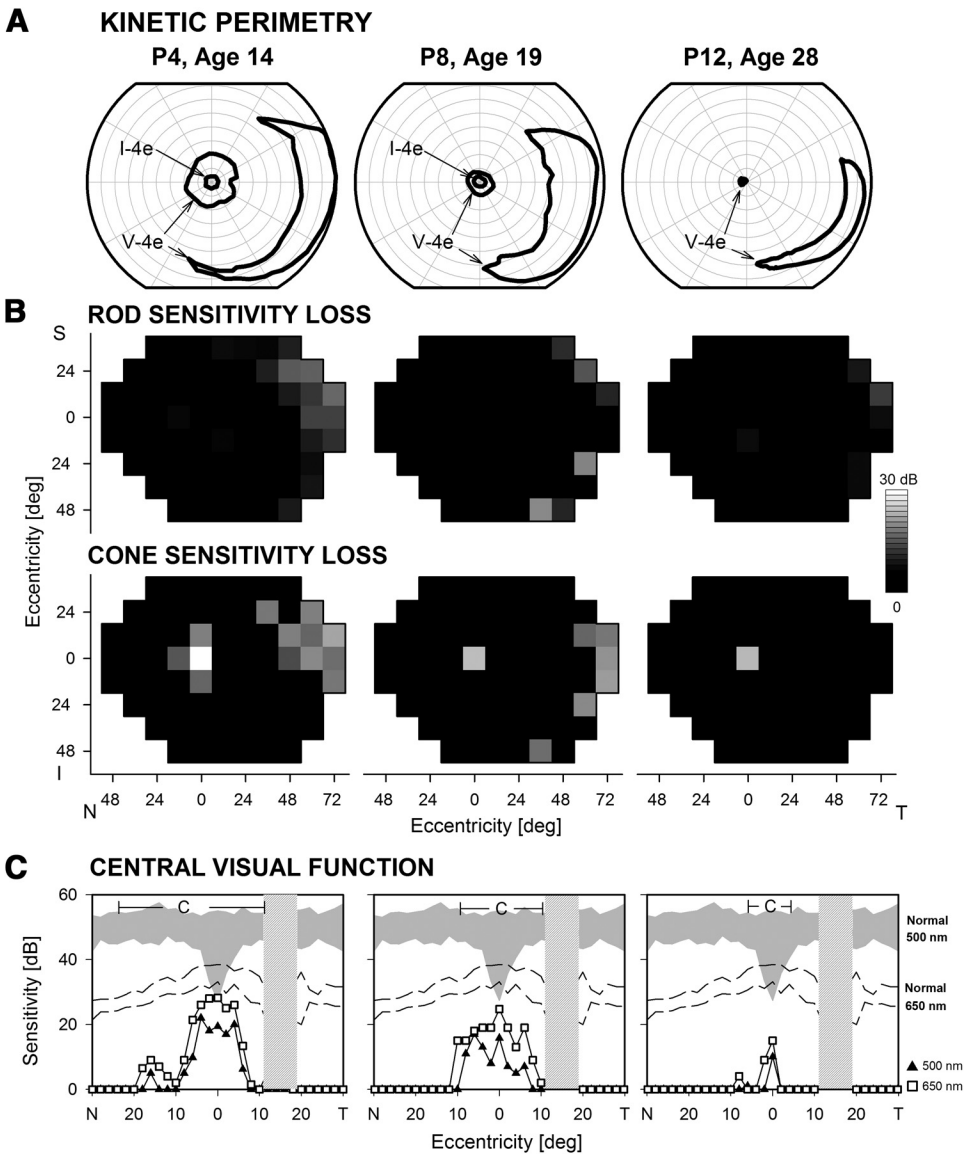

FIGURE 1. Visual function in representative patients with *CRB1*-RD. (**A**) Kinetic perimetry results using two targets (V-4e, I-4e) illustrate preserved central and temporal peripheral islands of vision. (**B**) Dark-adapted (*top*) and light-adapted (*bottom*) static threshold perimetry results displayed as grayscale maps of rod and cone sensitivity loss. The scale has 16 levels of gray, representing 0- to 30-dB losses. N, nasal; T, temporal; I, inferior; S, superior visual field. (**C**) Dark-adapted, two-color (500 and 650 nm) sensitivity profiles across the horizontal meridian (central 60°) in the patients (*symbols connected by lines*) compared with normal for rod-mediated sensitivity to the 500-nm stimulus (*shaded band*) and for cone-mediated sensitivity to the 650 nm stimulus at the cone plateau (*dashed lines*). The photoreceptor mediation at loci with function, based on the sensitivity difference between the two colors, is given: C, cone-mediated.

creased thickness with displaced inner retinal layers from foveal formation, a decline in thickness with eccentricity beyond this ring, and a prominent crescent-shaped thickening in the nasal retina extending into the superior and inferior poles of the optic nerve, attributable to the converging axons from ganglion cells. Thickness topography in two representative *CRB1*-RD patients (P4 and P12) showed abnormal thickening (at ages 16 and 28); retinal thickness in the central retina was >2 SD from normal mean thickness, except at and near the fovea (Fig 3A, lower right insets; pink is >2 SD, and white is within normal limits). Vertical cross sections through the fovea (±9 mm; total vertical expanse of ~60°) were analyzed in 19 of the 22 patients (data not shown). There was increased retinal thickness in all but two patients (P7 at ages 26 and 30; P18 at age 45), thus extending our previous observations in this population.[5] We also inquired whether there was a change in retinal thickness with age. Serial OCTs (across the vertical meridian, ±9 mm from the fovea) were available in five patients (P2, P4, P7, P8, and P12), each spanning a time interval of at least 4 years. P2 and P4 showed retinal thickness reductions between the ages of 12 and 19 years and 14 and 19 years, respectively. In contrast, P8 and P12 were monitored from ages 18 to 22 and 26 to 30 years, respectively, and there was no decrease in retinal thickness observed. All these patients, whether they showed progressive retinal thinning or not, continued to have hyperthickness at later time points. Of interest, P7, one of two patients with normal retinal thickness, was monitored between ages 24 and 30 years, and retinal thickness remained within normal limits at the later time point.

Regions of thickening in *CRB1*-RD retina, unlike in the well-laminated normal retina (Fig. 3B, left panel), showed coarse and abnormal layering[5] and many intraretinal hyperreflective structures (Fig. 3B, right panels). Hyperreflective lesions could be different in size and could be found at different depths from the vitreoretinal surface (Fig. 3B, arrows and arrowheads). Larger hyperreflective structures could be classified into at least two types based on OCT appearance: One type was associated with a shadowing of signal from deeper layers (Fig. 3B, P8 and P17, long arrows) whereas another type was associated with no detectable shadowing (P6, arrowhead). The shadowing features of smaller hyperreflective lesions were not as certain. Also notable in these scans was the lack of normal photoreceptor layers; and the regions in the retina depicted were associated with little or no measurable vision. We tested the hypothesis that the two types of larger hyperreflective lesions were associated with different en face appear-

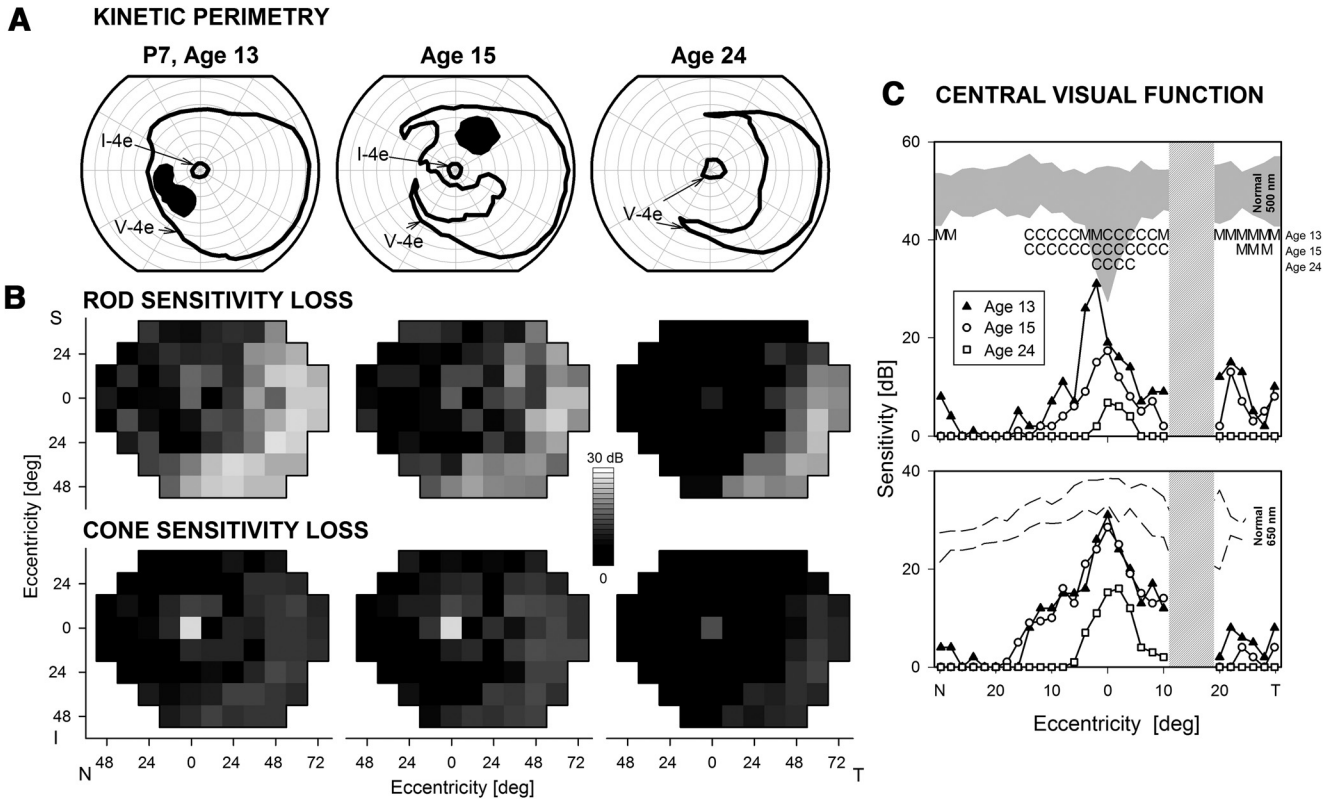

Figure 2. Longitudinal sequence of visual function in a *CRB1*-RD patient spanning 11 years. (**A**) Kinetic perimetry results in P7 at three ages. (**B**) Dark-adapted (*top*) and light-adapted (*bottom*) static threshold perimetry results displayed as grayscale maps of rod and cone sensitivity loss. Scale and labels as in Figure 1. (**C**) Dark-adapted two-color sensitivity profiles across the central 60° in P7 at the three ages. *Top*: sensitivity to the 500-nm stimulus compared with normal for rod-mediated sensitivity to this stimulus (*shaded band*). *Bottom*: sensitivity to the 650-nm stimulus compared with cone-mediated sensitivity to the same stimulus at the cone plateau (*dashed lines*). *Top graph*: photoreceptor mediation at loci with function: M, mixed rod (500 nm) and cone (650 nm) function; C, cone-mediated.

ance. OCT scans from nine patients (P2, P4, P5, P6, P10, P12, P15, P16, and P17) were studied to determine the relationship between the en face (SLO) and cross-sectional (OCT) image features. Hyperreflectivity with shadowing was associated with relatively darker lesions on en face images (Fig. 3C, left). These lesions are thought to correspond to pigment migration, including bone-spicule–like pigment and clumped pigmentary changes. Scattering and absorbing properties of melanin would explain the hyperreflectivity and the shadowing. On the other hand, hyperreflectivity without shadowing was associated with no apparent lesions or relatively brighter lesions on en face images (Fig. 3C, right). The basis of these scattering but nonabsorbing OCT features is less clear but could correspond to focal regions of dysplasia and pseudorosettes. Also notable were the hyperreflective abnormalities deep in the retina appearing proximate to the RPE or Bruch's membrane level of the scan (Fig 3B, P17, short arrows).

The unusually thickened parapapillary nerve fiber layer, we previously observed in *CRB1*-RD patients[5] and the limited literature on visual pathway integrity in LCA with known genotype[29] prompted study with MR to determine whether the visual brain is normal in *CRB1*-RD (Figs. 3D–F). Visual pathway structures in *CRB1*-RD patients appeared normal in MR images. The interpial optic nerve diameter in P8, P12, P11, and P22 (aged 21, 29, 34, and 53, respectively, at the time of the scan) was normal (Fig. 3D), as defined by measurements from our normal subjects and published data.[30] A voxel-based morphometric analysis[19] of the anatomic images obtained from four *CRB1*-RD patients tested whether atrophy was present within the occipital lobe white matter, as has been noted in patients with early-onset blindness of various causes.[31] The *CRB1*-RD patients fell within the range of control subject data; the *CRB1*-RD patient mean, however, was slightly but significantly reduced in comparison to that of the controls (log Jacobian [normed]: controls, 0 ± 0.03 SEM; *CRB1*-RD patients, −0.14 ± 0.06; t [31 *df*] = 2.2, $P = 0.04$ one-tailed), indicating relative atrophy of occipital white matter structures. The thickness of the cortical gray matter layer was measured within a striatal region of interest defined by cortical surface topology.[21] Increased striatal cortical thickness has been observed in previous studies of early-onset blindness[32] and attributed to the failure of developmental synaptic pruning. The gray matter layer was thicker in *CRB1*-RD patients than in the controls, but not significantly so (thickness in millimeters: controls, 1.67 ± 0.03 SEM; *CRB1*-RD patients, 1.87 ± 0.12; t [6 *df*] = 1.7; $P = 0.07$ one-tailed).

We assessed functional cortical responses to large-field light stimulation.[29] Whole-brain responses in *CRB1*-RD patients were of reduced amplitude and spatial extent compared with those in normally sighted controls (Fig. 3E). Within the posterior visual cortices (Fig. 3F), the volume of activated tissue was significantly reduced in *CRB1*-RD patients compared with that in controls (t [6 *df*] = 5.4; $P = 0.002$ one-tailed). The four *CRB1*-RD patients, ranked in order of higher to lower activation volume, were P8, P12, P11, and P22. The severity of retinal disease expression in these patients at the time of fMRI was compared by ranking central visual function. A ranking by visual acuity in the better eye and by dark- and light-adapted visual sensitivity in the central field mirrored the fMRI results,

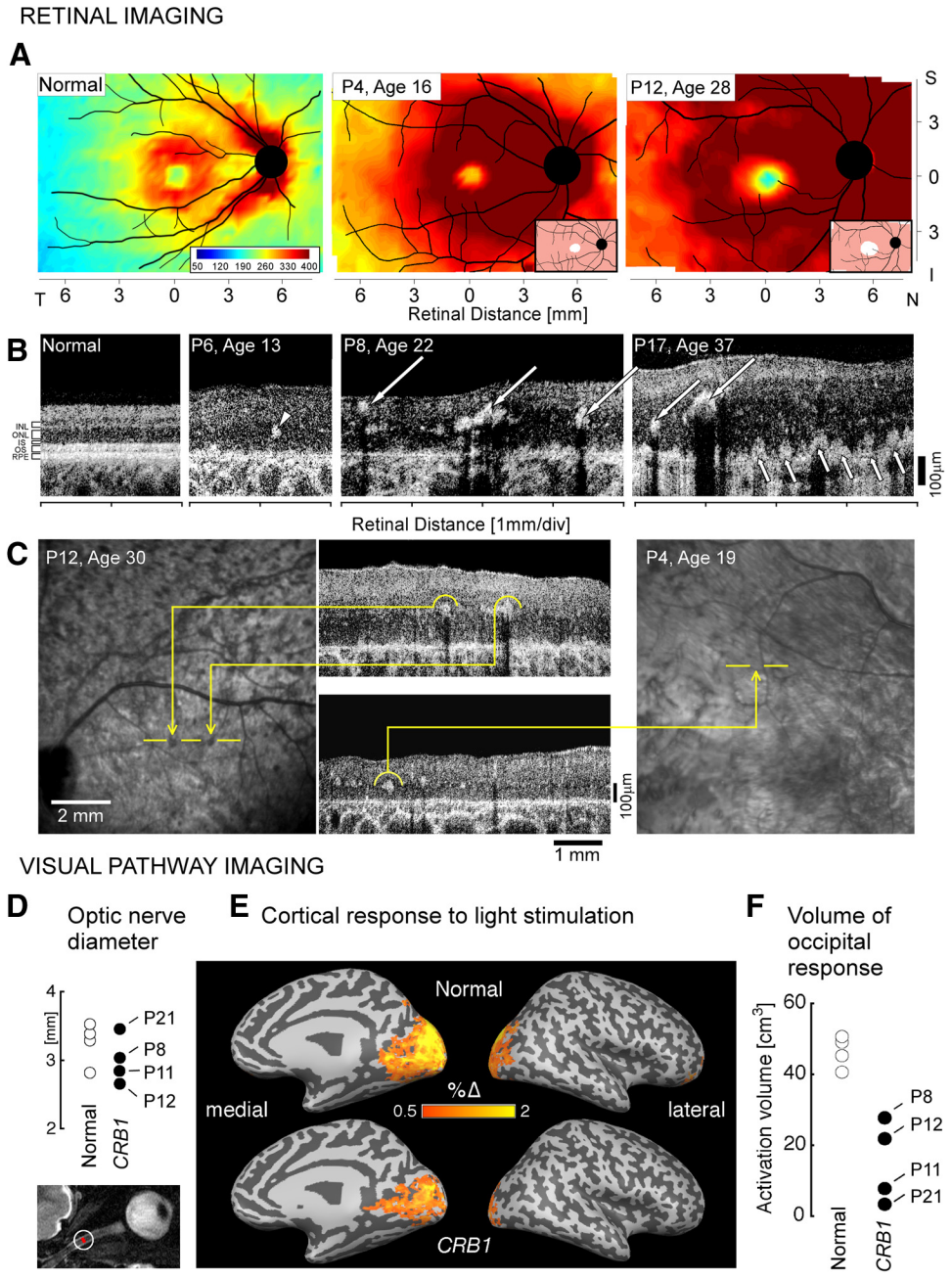

Figure 3. Retinal and visual pathway structure in *CRB1*-RD. (**A**) Topographical maps of retinal thickness in a normal 21-year-old subject (*left*) and two patients with *CRB1*-RD. Traces of major blood vessels and location of the ONH are overlaid on each map. Pseudocolor scales are shown. *Insets* in the patient maps, *bottom right:* thickness difference maps showing region that is within normal limits (*white*, defined as the mean ± 2 SD, $n = 5$), or thickened (*pink*, >2 SD), compared to normal. (**B**) Cross-sectional OCT images along the horizontal meridian in the temporal retina in a normal subject (*left*, age 24) compared to scans from three patients with *CRB1*-RD. *Arrowhead*: intraretinal hyperreflective structures without shadowing. *Large arrows*: hyperreflective structures with shadowing. *Small arrows*: hyperreflective lesions apparently extending from RPE vitread into the nuclear layer. (**C**) En face infrared reflectance images compared with OCT cross sections in two *CRB1*-RD patients to illustrate the relationship between intraretinal hyperreflective structures, with and without shadowing, and fundus features. In P12, two pigment clumps correspond to intraretinal hyperreflective structures with shadowing. In contrast, intraretinal hyperreflective structures without shadowing in P4 do not correspond to a discrete pigmentary change on the fundus image. (**D**) High-resolution T_2-weighted axial images obtained through the optic nerves. The cross-sectional diameter of the interpial optic nerve was estimated at two positions along each nerve (*inset*, axial image), and the average diameter was within the range of normal. (**E**) Cortical (BOLD fMRI) response to light stimulation is shown for normal subjects and *CRB1*-RD patients on a digitally inflated right hemisphere. *Dark gray*: sulci; *light gray*: gyri. The color scale indicates the percentage change of BOLD signal in response to light. Activation in occipital visual cortex is seen for both groups, but is reduced in *CRB1*-RD. (**F**) Volume of posterior cortical tissue demonstrating a substantial (2%) response to light stimulation was significantly greater in controls than in *CRB1*-RD patients.

with the least affected being P8 and in order of increasing visual loss: P12, P11, and P22.

Crb1-Mutant *rd8* Mice Show Patchy Dysplasia and Some Retinal Degeneration

ERG parameters were compared between *rd8* and age-matched WT control mice (Fig. 4A). All rod photoreceptor–driven ERG parameters, except for the dark-adapted maximum b-wave amplitude (V_{max}), showed no significant differences between *rd8* and WT for all grouped comparisons. For the oldest group of mice, V_{max} was significantly smaller than WT: mean (SD) in *rd8* = 180 (75) μV versus 278 (64) μV in WT (P = 0.002). In addition, one to three *rd8* eyes in each group showed responses that fell outside the range recorded in WT eyes. Cone responses elicited with white stimuli were not significantly different from WT (Fig. 4A). Further, responses to UV and green flashes in the light-adapted state did not show significant mismatches in the *rd8* group when compared to the WT group (UV-to-green difference: −11.7 [9] μV in *rd8*, −14.8 [18] μV in WT; P = 0.63), implying normal or near-normal short-wavelength (S) –and middle-wavelength (M)–sensitive cone function in *rd8* mice over the age range studied.

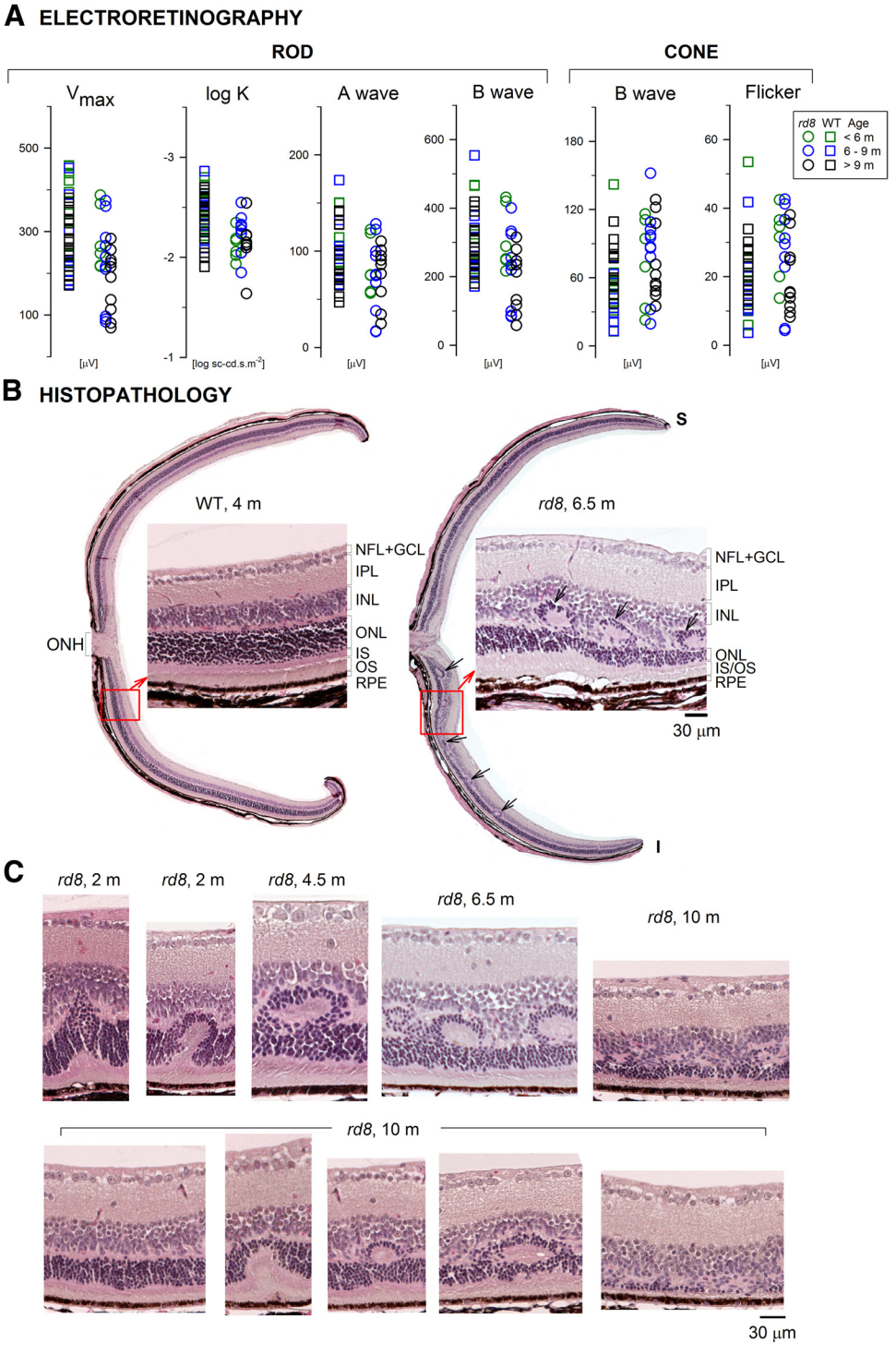

Figure 4. Retinal function and histopathology in the *Crb1*-mutant *rd8* mouse. (**A**) ERG parameters compared in a cohort of WT and *rd8* mice of different ages (key for color coding of ages, *right*). (**B**) Dorsal-ventral retinal sections in a 4-month-old WT mouse (*left*) compared with that of a 6.5-month-old *rd8* mouse. To the right of each full retinal section is a higher magnification light microscopic image from a location (*square with arrow*) inferior to the optic nerve. *Arrows*: dysplastic regions in the *rd8* histopathology. (**C**) Retinal sections with different abnormalities are ordered (*left* to *right*) in a proposed disease sequence leading to the types of dysplastic lesions noted in *rd8* animals of increasing ages (*top* images). Sections are shown from one animal at age 10 months (*bottom* images) to illustrate that the abnormalities can occur within a retina at a single age.

Dorsal-ventral histologic sections through the optic nerve are compared in a WT retina (age 4 months, left) and an *rd8* retina (age, 6.5 months, right; Fig. 4B). At low magnification, patches of dysplasia were present in the inferior (ventral) retina of the *rd8* mouse (arrows). Retinal sections at higher magnification, from inferior to the optic nerve in the WT and *rd8* retinas, are shown adjacent to the full dorsal–ventral sections. The WT section shows the normal architecture with well-defined nuclear layers (GCL, INL, and ONL), synaptic layers, the photoreceptor inner and outer segments, and the RPE. In the *rd8* section, the laminae were identifiable, but between the ONL and INL were retinal folds or pseudorosettes, as documented previously in *Crb1*-mutant mice.[8,9,33–36] Across the *rd8* section, there was an apparent variation in ONL and IS/OS thickness.

Sections from the inferior retina of *rd8* mice at different ages suggest a possible sequence of abnormalities leading to the dysplasia. Impaired adhesion between photoreceptors and MG cells (due to zonulae adherens junction abnormalities) and loss of OLM integrity have been shown to be early findings in *rd8* and other *Crb1*-mutant mouse models (for example, Refs. 9, 33, 34). Displacement of IS/OS material and photoreceptor cell bodies into the inner retina (Fig. 4C, age 2 months) could be the result of fragmentation of the OLM and loss of this normal structural barrier.[37] Repair processes that lead to readherence of MG and photoreceptor cells have been postulated to occur,[8] and this could lead to isolation of the pseudorosette between INL and ONL (Fig. 4C, 4.5 months). There appear to be variable numbers and sizes of pseudorosettes (Fig. 4B, right; Fig. 4C, 4.5 vs. 6.5 months). This variation may relate to the regional retinal extent of OLM integrity at different disease stages and the modulation of the fragmentation and repair processes by unknown factors.[34] This sequence of abnormalities displayed in *rd8* mice of increasing age (Fig. 4C, top) was also found in individual animals (Fig. 4C, lower row). A 10-month old *rd8* mouse, for example, showed, in inferior (ventral) sections, a similar spectrum of results: ranging from (left to right) no obvious dysplasia, to focal displacement of IS/OS material into ONL, to a formed pseudorosette, to more extensive or multiple pseudorosettes, to an amalgam of ONL and INL and retinal degeneration with reduced ONL thickness and IS/OS.

OCT scans were performed and quantified in 22 *rd8* mice and compared with those in 13 WT mice (Fig. 5). OCT cross sections were compared to histologic sections (Fig. 5A) from the inferior retina of WT and *rd8* mice. In the WT histology–OCT pair (Fig. 5A, left), the vitreoretinal interface was hyperreflective, and there were hyporeflective zones that represent the INL and ONL; the deep complex hyperreflectivity represents the IS, OS, RPE, and choroid.[15] Correspondence between retinal histology and OCT features has been quantified previously.[15,38–40] The *rd8* OCT sections also have identifiable vitreoretinal interface hyperreflectivity, INL and ONL hyporeflective layers, and a deep hyperreflective outer retinal complex. At a presumed early stage of pseudorosette formation with IS and OS material displaced into the ONL (see Fig. 4C), there was a hyperreflective region (arrow) with corresponding thinning of the ONL at that locus (Fig. 5A, middle pair). A more fully formed pseudorosette between ONL and INL (Fig. 5A, right pair) is illustrated histologically, and the OCT shows a hyperreflective region (arrowhead) between the INL and ONL with surrounding hyporeflectivity suggestive of the dysplastic lesion.

Representative vertical OCT scans across the ONH showed that there were hyperreflective abnormalities between the INL and ONL at all ages studied in the *rd8* animals (Fig. 5B). All *rd8* animals between the ages of 3 and 7 months ($n = 11$) showed abnormal hyperreflective structures in the OPL region (arrowheads), and some also had hyperreflective lesions that spanned the retina from the deep outer retinal complex into the ONL (arrow). Of the 10-month old *rd8* eyes, eight of nine showed such hyperreflectivity in the inferior retina and four of nine eyes showed similar abnormalities superiorly. The dramatic retinal thickening in human *CRB1*-RD[5] prompted us to analyze retinal thickness in the *rd8* retinas. Retinal thickness measurements of OCT vertical scans from each of three *rd8* age groups did not show remarkable differences compared with WT data (Fig. 5C). There was a reduction of *rd8* inferior retina thickness with age, whereas the superior retinas were relatively constant.

Prompted by the relatively normal ERGs in the *rd8* mice, we asked whether there was any evidence of outer retinal abnormalities, specifically the IS+OS thickness (Fig. 5D). ONL integrity, compromised by pseudorosette formation, was a less feasible target for morphometry. We compared IS+OS thickness in *rd8* ($n = 4$, one eye per animal, ages 4 and 6.5 months) and WT ($n = 2$, one eye per animal, age 4 months) mice. Eight histologic sections were used for each eye. Within each section, a single pair of measurements was performed at adjacent locations. In *rd8* eyes, adjacent areas with and without dysplastic changes (Fig. 5D, inset) were compared. There was a significantly thinner IS+OS in dysplastic regions ($P = 0.023$, ANOVA), and the mean difference from neighboring nondysplastic regions was 5.1 μm or 20% (Fig. 5D). There was no significant effect of age ($P = 0.99$, ANOVA), and there were no significant differences between WT eyes and nondysplastic regions of *rd8* eyes ($P = 0.73$, ANOVA).

Discussion

Human *CRB1* Phenotype

The cohort of *CRB1*-RD patients in the present study shared many features of their retinal degenerative disease, and the phenotype mainly varied in the degree of severity. Reports of phenotypic variability in *CRB1*-RD emphasize differences in clinical diagnoses (for example, LCA, juvenile-onset RP, or autosomal recessive RP) and fundus appearance among patients.[6] From another perspective, homogeneity of clinical disease presentation is not the rule in genetically defined autosomal recessive disease, even in patients from a genetically isolated population and from the same family (for example, Refs. 41, 42). We conclude that patients presenting with an early-onset presumed autosomal recessive retinal degenerative disease, retina-wide severe photoreceptor dysfunction by ERG, hyperopic refractive error, and retinal disorganization and thickening by OCT warrant consideration of genetic testing for causative mutations in the *CRB1* gene.

Our original observation of retinal thickening in *CRB1*-RD patients[5] has been debated[43,44] and confirmed.[6] The larger cohort of patients with OCT measurements and serial follow-up in the present study have led to the finding that two patients had retinal thickness that was within normal limits and that there can be retinal thinning with age in some patients. Those with documented progressive thinning were younger patients, but they continued to have hyperthick retinas at last measurement. The basis of the retinal thickening, which has now been documented in other forms of LCA (for example, Refs. 26, 45, 46) is uncertain, but a parsimonious explanation may be that it is an exaggerated remodeling process in some individuals. Given the MG cell defect in *CRB1* disease[9] and a possible proliferative response to early photoreceptor loss, this is plausible. Thinning may be part of the process of contraction of the MG reaction into a scar, as described in animal models.[47]

The pattern of visual field loss in *CRB1*-RD patients has not received much attention in earlier reports of phenotype. We

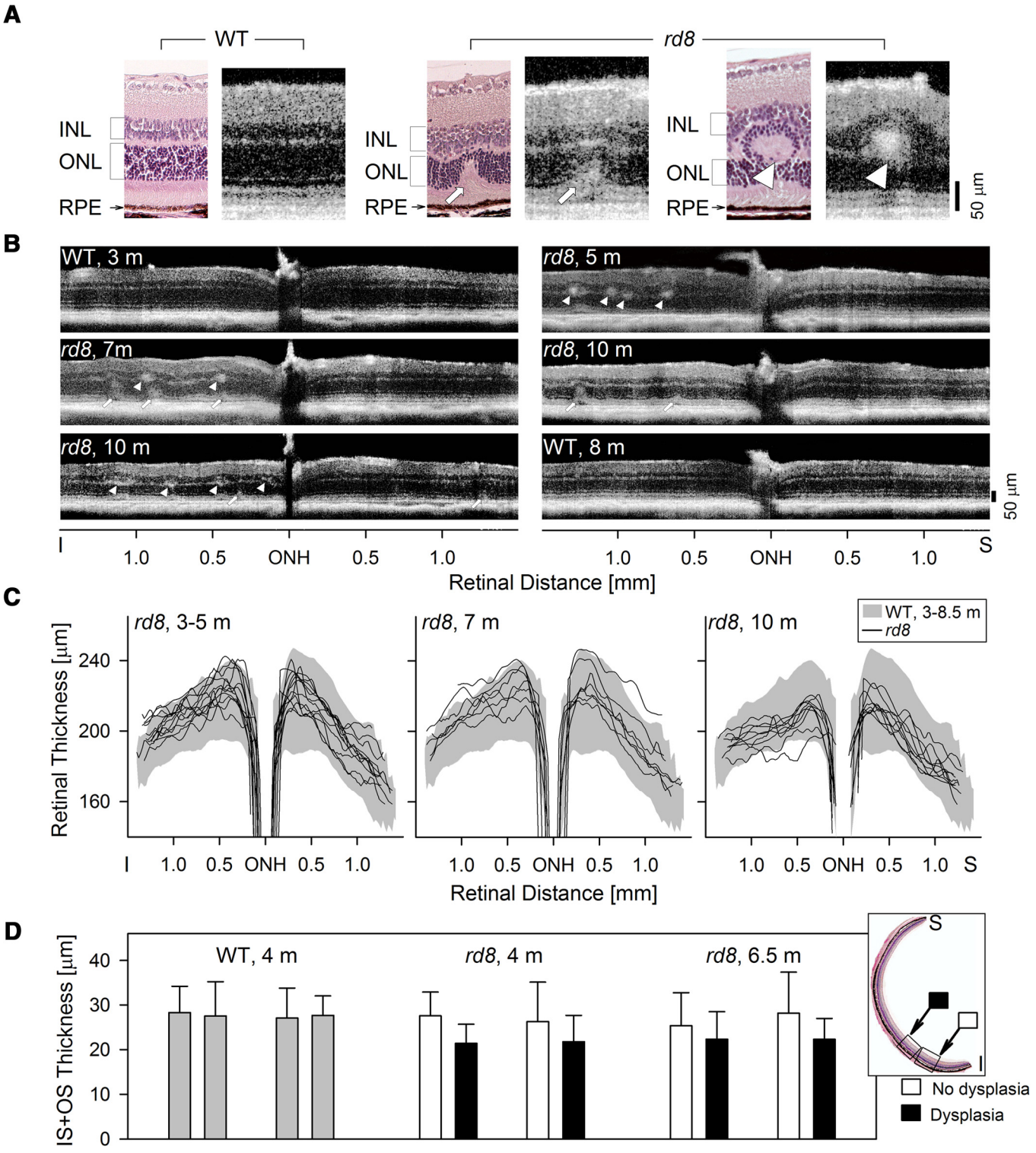

FIGURE 5. OCT analysis of the retinal abnormalities in *rd8* mice. (**A**) Histologic and OCT sections in WT (*left*) and *rd8* (*middle* and *right*) retinas to illustrate the relationship between the different modalities of determining laminar architecture and how abnormalities would appear with noninvasive optical imaging. *Left*: a 4-month-old WT retina histology section is compared to a 5-month-old WT OCT scan; *middle*, a 10-month-old *rd8* histology section is compared to a 10-month-old OCT image from another *rd8* animal; *right*, 6.5-month-old *rd8* histology section is compared to a 7-month-old *rd8* OCT scan. (**B**) Representative OCT scans across 3 mm of retina centered at the ONH, to illustrate detectable abnormalities, such as focal hyperreflective lesions at the level of the OPL (*arrowheads*) and deeper retinal hyperreflective lesions extending into the ONL (*arrows*), in the *rd8* animals. (**C**) Dorsal–ventral OCT sections quantified for retinal thickness in three different age groups of *rd8* mice. In the 3- to 5-month-old age group, 12 *rd8* eyes were analyzed; in the 7-month-old group, 7 eyes; and in the 10-month-old group, 9 *rd8* eyes. *Shaded bands*: the mean ±2 SD of retinal thickness in WT eyes ($n = 26$, ages 3–8.5 months). Data over this age range were grouped together based on linear regression analyses performed between retinal thickness and age at four selected locations (±0.5 mm and ±1 mm from ONH); slopes of the regression analyses were not significantly different from 0. (**D**) IS+OS thickness measurements in regions of dysplasia in *rd8* histologic sections are compared to adjacent nondysplastic regions (see *inset* for location of samples) for *rd8* mice (two animals each, 4 and 6.5 months old), and in similarly located regions in two WT mice (*gray bars*). Error bars, ±2 SD.

observed persistent peripheral visual function, even at relatively late disease stages when central vision is severely affected. The evidence of acceleration by exposure to light of the disease progress in *Crb1*-mutant mice[8,9,34] provokes the hypothesis that far peripheral islands may be in the shadow of the ciliary body, and this may help explain their persistence in human *CRB1*-RD. The present study of the visual pathways in *CRB1*-RD is the third study in LCA patients of known genotype.[29,48] In *CRB1*-RD patients, cortical responses to light were reduced and confined to early visual areas compared with those in controls. A similar attenuation of extrastriate cortex was reported in a patient with early anterior segment damage.[49] This reduction in *CRB1*-RD patients contrasts with the relative preservation of functional responses in patients with *RPE65*-LCA.[29] Differential impairments in *CRB1*-RD retinal function or developmental changes to visual cortex could account for this finding. The results suggest that more LCA patients of known genotypes should be similarly evaluated, considering the increasing interest in treating early-onset blinding retinal diseases.

Dysplasia in Mouse and Man: Similar or Different?

The retinal histopathology in *rd8* mice of different ages (up to 10 months) led to our suggestion of a sequence of abnormalities in laminar architecture. These observations confirm and extend those in previous reports of *Crb1*-mutant mice.[8,9,33] The disease sequence could be found, not only in animals of increasing ages, but also within the retina of the same animal. There was regional retinal predilection for the dysplasia, the inferior retina, but there were also adjacent regions in the inferior retina of normal appearance.[8,9,33,34] The retinal disorganization in Crb1 deficiency is thought to begin from defects in the OLM, leading from adhesion abnormalities between MG cells and photoreceptors.[50,51] Inner and outer segment material can be seen extending vitread beyond the OLM and into the ONL. Isolated or multiple pseudorosettes are identifiable between the ONL and INL, and there can also be regions in which ONL, pseudorosettes, and INL appear intermingled with poorly defined boundaries between laminae. At this stage of the process, the ONL is thinned, and IS+OS length is reduced. Our cross-sectional histopathology data suggest that this process is a dynamic one, but it is unknown why it occurs at certain retinal sites and at certain times in the life of an animal but not others. Evidence has been provided for acceleration but not induction of the process by light, for dependence on genetic background, and for the possibility that there are continuous repair processes and glial activation and scarring, making any simple interpretation of the disease sequence more complex.[8,9,33,34,36]

Is there a relationship between dysplasia and degeneration in the *rd8* mouse? Despite the retinal disorganization, ERG measures of retina-wide function, including photoreceptor (a-wave) responses, were generally normal. We compared the IS+OS length in delaminated retina and adjacent normal-appearing retina in the same animals. Of interest, the well-laminated retinal regions had IS+OS length that was within normal limits compared to age-matched control animal data from comparable regions of the inferior retina. The retinal regions with dysplasia (excluding areas with IS/OS material beginning to extend into the ONL that lead to artifactual measurements) had measurable but significantly reduced IS+OS length. This association of reduced IS+OS length with dysplastic regions suggests that retinal degeneration is a consequence of the disorganization. The patchy nature and altitudinal (inferior) retinal location of disorganized retina most likely explains why the ERG remains normal in most animals, with retinal function deriving from normal patches and functioning, albeit abnormal, dysplastic retina. We tested the hypothesis that the higher S-cone content of the inferior retina reveals a relative decrease in S-cone versus M-cone function in *rd8*,[34] but there was no such inequality of cone results.

A prominent difference between the human disease and the mouse model is the early and severe loss of retinal function in *CRB1*-RD compared with the near-normal retinal function in *rd8* mice. This functional difference is understandable in relation to retinal morphology. Human *CRB1*-RD retinas with mainly nondetectable ERGs and extensive midperipheral scotomas are coarsely thickened and delaminated without measurable ONL or IS/OS in extracentral regions, whereas *rd8* mice retain mainly normal retina in the superior retina and inferior retinal patches of normal or abnormal (but detectable) photoreceptor structure. At the ages we studied, the *rd8* mice did not manifest increased retinal thickness by OCT. Characterization with histopathology and OCT of the various lesions in the *rd8* retina also permits some further comparisons with human *CRB1*-RD. The human disease showed abnormal hyperreflective lesions of various sizes and retinal depths in regions of thickened, nonseeing retina. These hyperreflective lesions show some resemblance to those in *rd8* retinas and thus may represent images of pseudorosettes, as has been suggested for another retinopathy with this pathologic pattern.[52] Alternatively, they may be examples of the common pigment migration into the inner retina that occurs in various retinal degenerations.[53,54] Our sampling of OCT scans and en face images in *CRB1*-RD patients indicated that the larger intraretinal hyperreflective OCT lesions with shadowing of signal from deeper layers did co-register with pigmentary changes visible on en face images. Hyperreflective structures without shadowing were not related to pigmentary change and raise the suspicion that there may be pseudorosettes in human *CRB1*-RD. Of interest, a human donor eye with a molecularly undefined retinal degeneration did show pseudorosettes.[55] Evidence from the present study is provocative but not sufficient to determine whether the dysplastic lesions in the Crb1-deficient mice have a correlate in the human disease.

Implications for Therapeutic Intervention in This Form of LCA

The residual peripheral islands detected in most of the *CRB1*-RD patients, even in later stages of the disease, provide a target retinal region for treatment that would be inclusive of clinical diagnoses from LCA to RP. If the islands were able to persist longer or there was an increase in rod and/or cone sensitivity within them, it would make a major positive difference to the mobility of these patients. Our *rd8* observation of a sequence leading from dysplasia to degeneration prompts the speculation that this sequence may also be occurring in the human disease, albeit slower and with a different regional retinal predilection. A therapy would seek to interrupt the sequence so that the remaining peripheral (and central) retina does not progress to degeneration. The MG cell, specifically the subapical region, is the main site for Crb1,[9,50] whereas other members of the Crumbs protein complex are in both photoreceptor and MG cells. Whereas gene delivery to RPE cells via subretinal injection has been accomplished in human participants in clinical trials of one form of LCA (reviewed in Ref. 10), MG cells may be the targets for gene augmentation in *CRB1*-RD, and this could be accomplished by an intravitreal approach (for example, Ref. 56).

Given a potential therapeutic strategy in humans with *CRB1*-RD, we asked whether the *rd8* mouse, which derives from a spontaneous frameshift mutation in *Crb1* causing a premature truncation, is a sufficiently faithful replica of the

human disease to proceed to proof-of-concept studies. The constantly evolving and not apparently predictable foci of dysplastic disease, the large regions of apparently unaffected superior retina, and the lack of impact on photoreceptor function and structure (in the first 10 months of *rd8* life) suggest *rd8* would not produce the type of outcomes that could be readily assayed for treatment effects. The same is generally true of the two other mouse models explored to date: $Crb1^{-/-}$ knockout and $Crb1^{C249W/-}$ knockin mice.[8,9,34] It is of interest that preliminary reports of double-knockout mice (*Crb1* and *Crb2)* show a more severe phenotype and retina-wide disease distribution, indicating that there may be overlapping functions of some members of the Crumbs protein complex in the mouse retina but possibly not in the human one (Pellissier L, et al. *IOVS* 2011;52:ARVO E-Abstract 4339).

Acknowledgments

The authors thank Hongwei Yu for excellent technical support.

References

1. Bazellieres E, Assemat E, Arsanto JP, Le Bivic A, Massey-Harroche D. Crumbs proteins in epithelial morphogenesis. *Front Biosci.* 2009;14:2149–2169.
2. Heckenlively JR. Preserved para-arteriole retinal pigment epithelium (PPRPE) in retinitis pigmentosa. *Br J Ophthalmol.* 1982;66:26–30.
3. den Hollander AI, ten Brink JB, de Kok YJ, et al. Mutations in a human homologue of drosophila crumbs cause retinitis pigmentosa (RP12). *Nat Genet.* 1999;23:217–221.
4. Lotery AJ, Jacobson SG, Fishman GA, et al. Mutations in the CRB1 gene cause leber congenital amaurosis. *Arch Ophthalmol.* 2001;119:415–420.
5. Jacobson SG, Cideciyan AV, Aleman TS, et al. Crumbs homolog 1 (CRB1) mutations result in a thick human retina with abnormal lamination. *Hum Mol Genet.* 2003;12:1073–1078.
6. Henderson RH, Mackay DS, Li Z, et al. Phenotypic variability in patients with retinal dystrophies due to mutations in CRB1. *Br J Ophthalmol.* 2011;95:811–817.
7. Walia S, Fishman GA, Jacobson SG, et al. Visual acuity in patients with leber's congenital amaurosis and early childhood-onset retinitis pigmentosa. *Ophthalmology.* 2010;117:1190–1198.
8. van de Pavert SA, Kantardzhieva A, Malysheva A, et al. Crumbs homologue 1 is required for maintenance of photoreceptor cell polarization and adhesion during light exposure. *J Cell Sci.* 2004;117:4169–4177.
9. van de Pavert SA, Sanz AS, Aartsen WM, et al. Crb1 is a determinant of retinal apical müller glia cell features. *Glia.* 2007;55:1486–1497.
10. Cideciyan AV. Leber congenital amaurosis due to RPE65 mutations and its treatment with gene therapy. *Prog Retin Eye Res.* 2010;29:398–427.
11. Jacobson SG, Voigt WJ, Parel JM, et al. Automated light- and dark-adapted perimetry for evaluating retinitis pigmentosa. *Ophthalmology.* 1986;93:1604–1611.
12. Roman AJ, Schwartz SB, Aleman TS, et al. Quantifying rod photoreceptor-mediated vision in retinal degenerations: dark-adapted thresholds as outcome measures. *Exp Eye Res.* 2005;80:259–272.
13. Jacobson SG, Yagasaki K, Feuer WJ, Román AJ. Interocular asymmetry of visual function in heterozygotes of x-linked retinitis pigmentosa. *Exp Eye Res.* 1989;48:679–691.
14. Aleman TS, Cideciyan AV, Volpe NJ, Stevanin G, Brice A, Jacobson SG. Spinocerebellar ataxia type 7 (SCA7) shows a cone-rod dystrophy phenotype. *Exp Eye Res.* 2002;74:737–745.
15. Huang Y, Cideciyan AV, Papastergiou GI, et al. Relation of optical coherence tomography to microanatomy in normal and rd chickens. *Invest Ophthalmol Vis Sci.* 1998;39:2405–2416.
16. Jacobson SG, Aleman TS, Cideciyan AV, et al. Identifying photoreceptors in blind eyes caused by RPE65 mutations: prerequisite for human gene therapy success. *Proc Natl Acad Sci USA.* 2005;102:6177–6182.
17. Aleman TS, Cideciyan AV, Sumaroka A, et al. Retinal laminar architecture in human retinitis pigmentosa caused by rhodopsin gene mutations. *Invest Ophthalmol Vis Sci.* 2008;49:1580–1590.
18. Cideciyan AV, Aleman TS, Boye SL, et al. Human gene therapy for RPE65 isomerase deficiency activates the retinoid cycle of vision but with slow rod kinetics. *Proc Natl Acad Sci USA.* 2008;105:15112–15117.
19. Ashburner J, Friston KJ. Voxel-based morphometry: the methods. *Neuroimage.* 2000;11:805–821.
20. Avants BB, Schoenemann PT, Gee JC. Lagrangian frame diffeomorphic image registration: morphometric comparison of human and chimpanzee cortex. *Med Image Anal.* 2006;10:397–412.
21. Hinds OP, Rajendran N, Polimeni JR, et al. Accurate prediction of V1 location from cortical folds in a surface coordinate system. *Neuroimage.* 2008;39:1585–1599.
22. Aguirre GK, Zarahn E, D'esposito M. The variability of human, BOLD hemodynamic responses. *Neuroimage.* 1998;8:360–369.
23. Roman AJ, Boye SL, Aleman TS, et al. Electroretinographic analyses of RPE65-mutant rd12 mice: developing an in vivo bioassay for human gene therapy trials of leber congenital amaurosis. *Mol Vis.* 2007;13:1701–1710.
24. Aleman TS, LaVail MM, Montemayor R, et al. Augmented rod bipolar cell function in partial receptor loss: an ERG study in P23H rhodopsin transgenic and aging normal rats. *Vision Res.* 2001;41:2779–2797.
25. Cheng H, Aleman TS, Cideciyan AV, Khanna R, Jacobson SG, Swaroop A. In vivo function of the orphan nuclear receptor NR2E3 in establishing photoreceptor identity during mammalian retinal development. *Hum Mol Genet.* 2006;15:2588–2602.
26. Cideciyan AV, Rachel RA, Aleman TS, et al. Cone photoreceptors are the main targets for gene therapy of NPHP5 (IQCB1) or NPHP6 (CEP290) blindness: generation of an all-cone Nphp6 hypomorph mouse that mimics the human retinal ciliopathy. *Hum Mol Genet.* 2011;20:1411–1423.
27. Lyubarsky AL, Falsini B, Pennesi ME, Valentini P, Pugh EN Jr. UV- and midwave-sensitive cone-driven retinal responses of the mouse: a possible phenotype for coexpression of cone photopigments. *J Neurosci.* 1999;19:442–455.
28. Ruggeri M, Wehbe H, Jiao S, et al. In vivo three-dimensional high-resolution imaging of rodent retina with spectral-domain optical coherence tomography. *Invest Ophthalmol Vis Sci.* 2007;48:1808–1814.
29. Aguirre GK, Komáromy AM, Cideciyan AV, et al. Canine and human visual cortex intact and responsive despite early retinal blindness from RPE65 mutation. *PLoS Med.* 2007;4:e230.
30. Karim S, Clark RA, Poukens V, Demer JL. Demonstration of systematic variation in human intraorbital optic nerve size by quantitative magnetic resonance imaging and histology. *Invest Ophthalmol Vis Sci.* 2004;45:1047–1051.
31. Ptito M, Schneider FC, Paulson OB, Kupers R. Alterations of the visual pathways in congenital blindness. *Exp Brain Res.* 2008;187:41–49.
32. Jiang J, Zhu W, Shi F, et al. Thick visual cortex in the early blind. *J Neurosci.* 2009;29:2205–2211.
33. Mehalow AK, Kameya S, Smith RS, et al. CRB1 is essential for external limiting membrane integrity and photoreceptor morphogenesis in the mammalian retina. *Hum Mol Genet.* 2003;12:2179–2189.
34. van de Pavert SA, Meuleman J, Malysheva A, et al. A single amino acid substitution (Cys249Trp) in Crb1 causes retinal degeneration and deregulates expression of pituitary tumor transforming gene Pttg1. *J Neurosci.* 2007;27:564–573.
35. van Rossum AG, Aartsen WM, Meuleman J, et al. Pals1/Mpp5 is required for correct localization of Crb1 at the subapical region in polarized Muller glia cells. *Hum Mol Genet.* 2006;15:2659–2672.
36. Pearson RA, Barber AC, West EL, et al. Targeted disruption of outer limiting membrane junctional proteins (Crb1 and ZO-1) increases integration of transplanted photoreceptor precursors into the adult wild-type and degenerating retina. *Cell Transplant.* 2010;19:487–503.
37. Omri S, Omri B, Savoldelli M, et al. The outer limiting membrane (OLM) revisited: clinical implications. *Clin Ophthalmol.* 2010;4:183–195.

38. Huang Y, Cideciyan AV, Alemán TS, et al. Optical coherence tomography (OCT) abnormalities in rhodopsin mutant transgenic swine with retinal degeneration. *Exp Eye Res.* 2000;70:247–251.
39. Fischer MD, Huber G, Beck SC, et al. Noninvasive, in vivo assessment of mouse retinal structure using optical coherence tomography. *PLoS One.* 2009;4:e7507.
40. Knott EJ, Sheets KG, Zhou Y, Gordon WC, Bazan NG. Spatial correlation of mouse photoreceptor-RPE thickness between SD-OCT and histology. *Exp Eye Res.* 2011;92:155–160.
41. van den Born LI, van Soest S, van Schooneveld MJ, Riemslag FC, de Jong PT, Bleeker-Wagemakers EM. Autosomal recessive retinitis pigmentosa with preserved para-arteriolar retinal pigment epithelium. *Am J Ophthalmol.* 1994;118:430–439.
42. Banin E, Bandah-Rozenfeld D, Obolensky A, et al. Molecular anthropology meets genetic medicine to treat blindness in the North African Jewish population: human gene therapy initiated in Israel. *Hum Gene Ther.* 2010;21:1749–1757.
43. McKay GJ, Clarke S, Davis JA, Simpson DA, Silvestri G. Pigmented paravenous chorioretinal atrophy is associated with a mutation within the crumbs homolog 1 (CRB1) gene. *Invest Ophthalmol Vis Sci.* 2005;46:322–328.
44. Simonelli F, Ziviello C, Testa F, et al. Clinical and molecular genetics of Leber's congenital amaurosis: a multicenter study of Italian patients. *Invest Ophthalmol Vis Sci.* 2007;48:4284–4290.
45. Jacobson SG, Cideciyan AV, Aleman TS, et al. RDH12 and RPE65, visual cycle genes causing leber congenital amaurosis, differ in disease expression. *Invest Ophthalmol Vis Sci.* 2007;48:332–338.
46. Jacobson SG, Aleman TS, Cideciyan AV, et al. Leber congenital amaurosis caused by Lebercilin (LCA5) mutation: retained photoreceptors adjacent to retinal disorganization. *Mol Vis.* 2009;15:1098–1106.
47. Jones BW, Marc RE. Retinal remodeling during retinal degeneration. *Exp Eye Res.* 2005;81:123–137.
48. Cideciyan AV, Aleman TS, Jacobson SG, et al. Centrosomal-ciliary gene CEP290/NPHP6 mutations result in blindness with unexpected sparing of photoreceptors and visual brain: implications for therapy of Leber congenital amaurosis. *Hum Mutat.* 2007;28:1074–1083.
49. Fine I, Wade AR, Brewer AA, et al. Long-term deprivation affects visual perception and cortex. *Nat Neurosci.* 2003;6(9):915–916.
50. Gosens I, den Hollander AI, Cremers FP, Roepman R. Composition and function of the Crumbs protein complex in the mammalian retina. *Exp Eye Res.* 2008;86:713–726.
51. Bulgakova NA, Knust E. The Crumbs complex: from epithelial-cell polarity to retinal degeneration. *J Cell Sci.* 2009;122:2587–2596.
52. Wang NK, Fine HF, Chang S, et al. Cellular origin of fundus autofluorescence in patients and mice with a defective NR2E3 gene. *Br J Ophthalmol.* 2009;93:1234–1240.
53. Li ZY, Possin DE, Milam AH. Histopathology of bone spicule pigmentation in retinitis pigmentosa. *Ophthalmology.* 1995;102:805–816.
54. Jaissle GB, May CA, van de Pavert SA, et al. Bone spicule pigment formation in retinitis pigmentosa: insights from a mouse model. *Graefes Arch Clin Exp Ophthalmol.* 2010;248:1063–1070.
55. Milam AH, Jacobson SG. Photoreceptor rosettes with blue cone opsin immunoreactivity in retinitis pigmentosa. *Ophthalmology.* 1990;97:1620–1631.
56. Klimczak RR, Koerber JT, Dalkara D, Flannery JG, Schaffer DV. A novel adeno-associated viral variant for efficient and selective intravitreal transduction of rat Müller cells. *PLoS One.* 2009;4:e7467.